Probing the interaction of noble gases with pristine and nitrogen-doped graphene through Raman spectroscopy

Renato Cunha, Néstor Perea-López, Ana Laura Elías, Kazunori Fujisawa, Victor Carozo, Simin Feng, Ruitao Lv, Maria Cristina dos Santos, Mauricio Terrones, and Paulo T. Araujo

Phys. Rev. B **97**, 195419 — Published 14 May 2018

DOI: 10.1103/PhysRevB.97.195419

Probing the Interaction of Noble Gases with Pristine and Nitrogen Doped Graphene through Raman Spectroscopy

Renato Cunha,[*,†,‡,¶] Néstor Perea-López,[†,‡] Ana Laura Elías,[†,‡] Kazunori Fujisawa,[†,‡] Victor Carozo,[†,‡,§] Simin Feng,[†,‡] Ruitao Lv,[!] M. C. dos Santos,[&] Paulo T. Araujo,[*,%,□] and Mauricio Terrones[*,†,§,‡,□]

[†] *Department of Physics, The Pennsylvania State University, University Park, PA 16802, USA*

[‡] *Center for 2-Dimensional and Layered Materials, The Pennsylvania State University, University Park, PA 16802, USA*

[¶] *Faculdade de Ciências Exatas e Naturais, Universidade Federal do Pará, Campus Universitário de Tocantins, PA 68.400-000, Brazil*

[§] *Department of Physics, Pontical Catholic University of Rio de Janeiro, Rio de Janeiro, RJ 22451900, Brazil*

[!] *Key Laboratory of Advanced Materials (MOE), School of Materials Science and Engineering, Tsinghua University, Beijing, 100084, P. R. China*

[&] *Zernike Institute for Advanced Materials, University of Groningen Nijenborgh 4, Groningen 9747 AG, The Netherlands*

[%] *Department of Physics and Astronomy, The University of Alabama, Tuscaloosa, AL 35487, USA*

[□] *Center for Information Technology (MINT), The University of Alabama, AL, 35487, USA.*

[§] *Department of Chemistry, The Pennsylvania State University, University Park, PA 16802, USA*

[□] *Institute of Carbon Science and Technology, Shinshu University, 4-17-1 Wakasato, Nagano-city 380-8553, Japan*

E-mail: mut11@psu.edu, jrenato@ufpa.br, paulo.t.araujo@ua.edu

Abstract

The interactions of adsorbates with graphene have received increasing attention due to its importance in the development of applications involving graphene-based coatings. Here, we present a study of the adsorption of noble gases on pristine and nitrogen-doped graphene. Single-layer graphene samples were synthesized by chemical vapor deposition (CVD) and transferred to transmission electron microscopy (TEM) grids. Several noble gases were allowed to adsorb on the suspended graphene substrate at very low temperatures. Raman spectra show distinct frequency blue shifts in both the 2D- and G-bands, which are induced by gas adsorption onto high quality single layer graphene (1LG). These shifts, which we associate with compressive biaxial strain in the graphene layers induced by the noble gases, are negligible for nitrogen-doped graphene. Additionally, a thermal depinning transition, which is related to the desorption of a noble gas layer from the graphene surface at low temperatures (ranging from 20 to 35K), was also observed at different transition temperatures for different noble gases. These transition temperatures were found to be 25K for Argon and 35K for Xenon. Moreover, we were able to obtain values for the compressive biaxial strain in graphene induced by the adsorbed layer of noble gases, using Raman spectroscopy. Ab initio calculations confirmed the correlation between the noble gas-induced strain and the changes in the Raman features observed.

Keywords: Raman spectroscopy**,** Graphene monolayer, physical adsorption, compressive strain, depinning, nitrogen doping.

1. Introduction

The adsorption of noble gases on various surfaces, including carbon nanostructures, is a very active research field, as it provides manageable model systems that can deepen the understanding of physical adsorption of atoms onto crystalline surfaces[1,2]. The adsorption process of noble gases on surfaces provides a probe for thermodynamic properties of systems with reduced dimensionalities (i.e restricted to at least one dimension), where new physics related to quantum confinement can be properly investigated. For instance, the formation of Bose-Einstein condensates and atomic super fluidity on surfaces can be studied using this model[3,4]. Many theoretical works[5-9] have been published regarding the adsorption of gases such as argon (Ar), krypton (Kr) and xenon (Xe) on single layer graphene (1LG or hereafter graphene), which are suitable substrates to study different phases of gas adsorbents. Noble gases when adsorbed in different surfaces also lead to a range of interesting phenomena such as a first order phase transition of Kr from two dimensional (2-D) vapor to commensurate solid, on individually suspended carbon nanotubes[10]. Noble gases on exfoliated bulk graphite also exhibit an excellent platform for a broad range of 2-D phenomena within the first adsorbed layer, including 2-D melting, transitions between solid phases, which might be either commensurate or incommensurate with the exfoliated graphitic lattice, and critical behavior of the adsorbents[2,11]. Adsorption can also be used for separation of gaseous mixtures[12], which is a viable industrial process where one component can be selectively adsorbed relative to others.

Schedin *et al.*[13] demonstrated that micrometer-size sensors made of graphene can detect individual gas molecules. The adsorbed molecules can easily change the local carrier concentration in graphene thereby changing its resistance. Moreover, graphene is an exceptionally low-noise material when it comes to its electronic properties, which is relevant to transport and optical applications, thus making it a promising candidate for the fabrication of chemical detectors[13]. The understanding of the interactions between adsorbate species and graphene is therefore very important for the advancement of graphene applications in such chemical-sensor devices. In contrast to carbon nanotubes (CNTs), graphene is a 2-D system with a large surface area that can be controlled during the graphene synthesis. Graphene Samples with an area much larger than 1 cm x 1 cm can be synthesized and it only depends on the size of original Cu foil used for the

synthesis. Very large surface areas are desirable as the efficiency of chemical reactions is proportional to surface area sizes[2,11].

Molecular Dynamics (MD) calculations usually assume that the strength of the van der Waals interactions between noble gases and carbon follows the order Xe > Kr > Ar[8,14], based on the binding energies measure for noble gases adsorbed on graphite.[2] Note that classical molecular dynamics calculations assumes an interaction strength between the surface and the adsorbate, which means that experiments are highly desirable to validate such MD calculations. Moreover, the interaction between carbon nanostructures and highly polarizable atoms such as Xe is significant, and leads to an appreciable adsorption, even at very low pressures[15]. It is also known that the surface binding energies depend on the substrate geometries, which are different for different crystals and crystallographic directions[2,11]. Defects are usually seen as imperfections in materials that could significantly degrade their performance. However, at the nanoscale, defects could be extremely useful since they could be exploited to generate novel, innovative and useful materials and devices. We will discuss in this paper doping defects, where the graphene lattice can be substitutionally doped by N atoms. Substitutional doping implies that the carbon atoms in the hexagonal lattice are substituted with dopants (e.g. N, B, P, S), whose incorporation into the lattice would perturb the sp^2 hybridization of the carbon atoms, and would cause significant changes to the electronic properties of graphene[16,17]. The use of various gases and adsorption surfaces will, therefore, lead to significant differences in adsorption potentials and binding energies[2,11].

Here, we investigate the adsorption of Ar, Kr, and Xe on single-layer pristine graphene (PG) and nitrogen-doped graphene (NG) at temperatures ranging from 20 to 50 K. Such temperature range has been poorly investigated in the literature, despite its importance for the formation of condensed two-dimensional phases of many simple gases[2]. We first obtained the Raman spectra of PG and NG with Ar, Kr, and Xe adlayers adsorbed to their surfaces. Our results show distinct shifts in the vibrational frequencies of PG although no shifts were observed in the NG Raman spectra. It is noteworthy that the shifts observed in the PG spectra are highly dependent on the adsorbed noble gas species. As it has been widely discussed, Raman spectroscopy is one of the most sensitive, informative and nondestructive spectroscopic techniques to analyze nanostructures, particularly carbon nanostructures[18,19]. This method has proven very

successful in monitoring phonons in a broad range of graphitic materials including graphene and SWCNTs[18,19]. In our experiments, significant blueshifts in the frequencies of the Raman features have been detected. For Xe adlayers adsorbed onto PG (Xe/PG) at 20K, the *2D*-band (also known as *G'*-band) blueshifts 8.4 cm^{-1} and the *G*-band blueshifts 1.8 cm^{-1}. These respective shifts are smaller in magnitude in the Ar/PG and Kr/PG systems. However, no significant shifts were seen in the Raman spectra frequencies related to the adsorption of these gases on NG at 20 K, Moreover, evidence of adlayers depinning has also been observed when increasing the temperature of the adsorbate/graphene systems. We hypothesize that the blueshifts observed for the Raman frequencies are mostly related to compressive biaxial strain in the graphene layers due to the presence of the adsorbates, a hypothesis that seems to be well explained by first-principles density functional theory (DFT) calculations, as discussed later in the text. Our results are also in good agreement with previous quartz crystal microbalance experiments related to adsorption of rare gases on graphene[20,21].

2. Methods

2.1. Experimental. PG and NG sheets were synthesized on copper foil in an ambient pressure chemical vapor deposition (AP-CVD) system[16] and transferred directly to a transmission electron microscopy (TEM) metallic grid, in order to obtain a suspended graphene sample and thus avoid the interaction with the substrate. This has been accomplished by the polymethyl methacrylate (PMMA) - assisted transfer method. The TEM metalic grid is a perforated ultrathin carbon film (less than 3nm thick) supported by a 300 mesh gold grid. The size of the holes in the carbon film are generally in the range of 1 μm to 2 μm, which gives the equivalent support of at least 6000 mesh grid. Both PG and NG samples were synthesized under similar experimental conditions, except for the introduction of ammonia (NH_3) for the case of NG[16,17]. Figure 1(a) shows transmission electron microscopy (TEM) images of monolayer NG sheets transferred to TEM grids via PMMA-methods and inset shows the corresponding selected-area electron diffraction (SAED) pattern of NG sheets, confirming the hexagonal structure of graphene. Details of the synthesis and transfer procedures of (PG) and (NG) monolayer can be found in our previous reports[16,17]. By the synthesis method used, which is thoroughly reported in an earlier publication by Lv et al[16]. we notice that the NG sample contains both double substitution N doping (N_2^{AA}), which is a double

substitution of N in a single C ring as can be seen in a model image in Fig. 1 (b), and single substitution, which is called N_1 configuration (shown in a model image in Fig. 1 (c)). Figure 1d shows a model image of the PG configuration. The double substitution N_2^{AA} is dominant. Indeed, Lv et al.[16] showed that according to the obtained X-ray photoelectron spectroscopy (XPS) data, about 90% of the N atoms inserted in the graphene lattice assumes the N_2^{AA} configuration. Detailed scanning tunneling microscopy (STM) images also show the same trend. Although the single substitution is present, it just plays a perturbative role when compared to the dominant N_2^{AA} configuration.

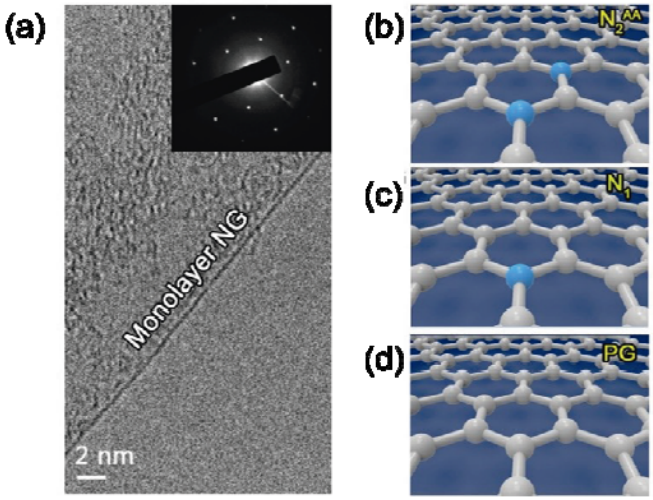

Fig. 1. (a) High-resolution transmission electron microscopy (HRTEM) and selected-area electron diffraction (SAED) pattern (inset) of monolayer NG sheet on TEM grid with holes in the range of 1 to 2 μm. ((b) and (c)) Models of (b) N_2^{AA} and (c) N_1 nitrogen doping configurations. (d) Model of PG without any nitrogen doping.

The experimental set-up consists of a liquid helium cryostat in which the TEM grid with the graphene materials is placed. This plate is pumped with a mechanical-turbo pump. The gas adsorption was performed at very low temperatures (from 20K to 50K) in which the gas flow was controlled by a mass flow controller (MFC). Next, Raman spectroscopy on suspended graphene monolayer was performed using a Renishaw inVia microscope-based Raman spectrometer. The spectra were collected in a backscattering geometry using 514.5 nm (2.41 eV) excitation wavelength. The incident

beam was focused through the window of the chamber in the sample surface with a microscope objective (Olympus 50x) and the back-scattered light was collected with the same objective. The measurements were performed using very low laser power densities in order to avoid the effect of laser-heating. No laser power dependence of the Raman spectra of the samples was observed for power densities < 0.5 mW/μm^2.

The schematic of the experimental set-up is shown in Fig. 2(a). Before starting the measurements by lowering the temperature we ran for a couple of hours a flow of H_2 in order to expel contaminants from the chamber. For the measurements at 20K under vacuum the MFC is closed and the pressure inside the chamber is kept around 10^{-6} Torr, whereas for the measurements with gas adsorption the valve of the vacuum pump is closed and the MFC is opened for a few seconds so that the gas is slowly admitted into the chamber which is now set at the desired temperature (from 20K to 50K) increasing the pressure to ~ 10^{-3}Torr. The measurements were performed after the samples reached thermal equilibrium with the chamber's temperature.

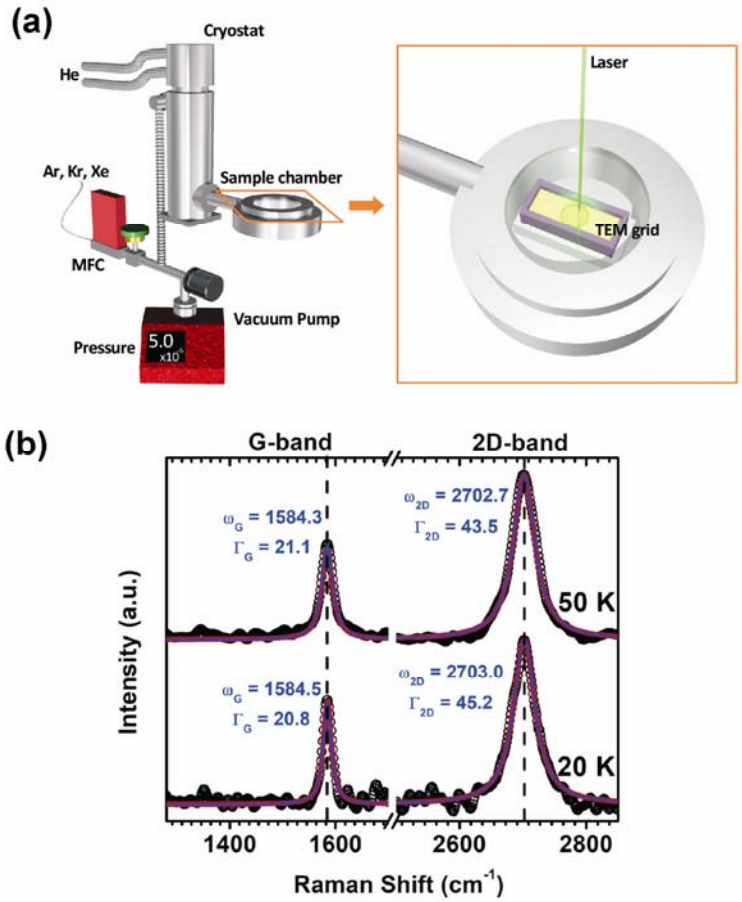

Fig. 2. (a) Schematic set-up of the experiment showing gas admission into the chamber at low temperature. (b) PG spectra collected at 20K and 50K. Note that no meaningful changes in frequency and

linewidth are observed. The black bullets are the experimental data and the solid lines are the fitting results (red) and the Lorentzian curves (blue) used to fit the data. The experimental errors for the frequencies and linewidths are, respectively, ±0.5 and ±1.

All of our spectra were carefully fitted with Lorentzian curves after appropriate baselines were taken. No treatments of the raw data, such as smoothening or interpolation/extrapolation were performed. All the frequency values reported here were extracted from the fitting results. The fitting procedure was repeated several times and with different data in order to increase accuracy. On top of that, the Raman spectrometer used here has a resolution of about 1.0 cm^{-1} or less and it can measure frequency shifts with an accuracy of ± 0.3 cm^{-1}. As shown in Fig. 2(b), the PG spectra collected at 20K and 50K show no meaningful changes in frequency and linewidth, which indicates that thermal effects are not the phenomena behind the spectroscopic changes due to noble gas adsorption, as discussed later in the text (see the Supplemental Material for a more detailed discussion [22]).

2.2. Computational Details. The interactions of the noble gases Ar, Kr, and Xe with graphene were studied by Density Functional Theory methods and two different approaches. The first approach used the meta-GGA (Generalized Gradient Approximation) functional M06L[23], which intrinsically includes dispersion. Gaussian type atomic basis sets were adopted, being 6-31G(d,p) for C and cc-pVDZ-F12[24,25] for Ar, Kr, and Xe. For the heavier Kr and Xe atoms, Electron Core Potentials (ECP) with relativistic corrections[26] were used. Calculations were carried out with two-dimensional (2D) periodic boundary conditions (PBC) on supercells that included (i) a 5×5 graphene cell (50 C atoms) with 9 adsorbed Ar atoms or 7 adsorbed Xe atoms; (ii) a 3×3 graphene cell (18 C atoms) with 3 adsorbed Kr atoms; (iii) a 10×10 graphene cell (200 C atoms) with 36 Ar, or 32 Kr, or 29 Xe. Ground state geometries were obtained within the GAUSSIAN 09 (G09) code[27]. The k-point mesh was the default from G09 in all calculations (typically 34 points mesh in the smaller supercells and 10 points mesh in the larger ones). The second approach was carried out for the same 10×10 graphene cells described in (iii) but using three-dimensional (3D) PBC. In all cases the periodic box is 40 Å long in the direction perpendicular to the graphene plane. The GGA functional by Perdew-Burke-Ernzerhof (PBE)[28] with the semi-empirical dispersion correction of Tkatchenko and Scheffler (TS)[29] was used in combination with a plane

wave expansion of Kohn-Sham crystal orbitals, with a cut-off kinetic energy of 680 eV. Norm-conserving pseudo-potentials in the reciprocal space representation were used. These calculations were carried out using CASTEP software[30] as implemented in Materials Studio package[31]. The overall accuracy, in terms of k-point mesh and convergence criteria, was that of the "Fine" selection in CASTEP. No symmetry constraints were used in the above described calculations. For comparison purposes, the geometry of graphene was optimized using both calculations schemes. For the M06L method, the C-C bond length optimizes to 1.421 Å and the primitive cell vectors have a length of 2.461 Å, while the PBE-TS results are, respectively, 1.424 Å and 2.466 Å. Both optimized geometries lead to a perfectly planar graphene. The 2D lattice of the noble gases was also optimized by the M06L method. The resulting triangular lattices have interatomic distances of 3.832 Å for Ar, 4.086 Å for Kr, and 4.481 Å for Xe, and respective atomic densities of 0.078 at/Å^2, 0.069 at/Å^2, and 0.057 at/Å^2.

3. Results and discussion

Figure 3(a) shows the Raman spectra from the suspended PG sample at 20K, before and after the noble gases adsorption. The most notable features of the spectra are the first-order Raman band, called G-band, which corresponds to the doubly degenerate E_{2g} phonons (in-plane TO and LO phonons) at the Brillouin-zone center (Γ point), and the second-order Raman mode termed 2D-band that involves TO phonons near the K (K') points of the Brillouin zone (also shown in Fig. 3(b)). As observed in Figs. 3(a) through (c), the G- and 2D-band frequencies blueshift with magnitudes that depend on the noble gas adsorbed on graphene. It is noticeable that the shifts for the 2D-band are considerably higher than those of the G-band. This result is expected because the 2D-band is an inter-valley second order Raman scattering process which involves two identical phonons with non-null momentum that are resonantly scattered to connect inequivalent K and K' points back and forth (their wave vectors are determined by the relative distance of the K and K' Dirac cones and by the laser excitation energy.)[32-38]. In fact, phonons from zone-edge (around the K or K' points in the Brillouin zone) are more sensitive to external perturbations such as doping or strain than zone center phonons (around the Γ point in the Brillouin zone)[32,33,37] . The G-band is a first order process, which involves just one phonon with null momentum (it happens at the Γ-point). It is interesting to emphasize that, by taking into account the experimental error,

although changes in the frequencies are observed, no significant changes were observed for the linewidths and intensities of the G- and 2D-peaks. It is worth mentioning that the amount of gas atoms injected is enough to complete coverage of 1LG. These experiments were repeated several times by increasing the amount of gas injected to ensure a higher density of noble gas adsorption. For all the experiments starting from the fully covered graphene layer, we have observed Raman shifts very similar to each other. Therefore the shifts seem not depend on the density of the noble gas. Moreover, as mentioned above no changes in frequencies are observed in the range of temperatures between 20K and 50K (Fig. 2(b)). This suggests that these two factors, density variation and temperature are not the reason behind the blueshifts we observe.

Another way to explain our observations would be to correlate them to doping processes during the adlayer adsorption. However, we discard this possibility for two reasons: **(1)** the adlayers are formed with noble gases, which are neutral and very stable so the likelihood of having them ionized under the experimental conditions presented here is low, and **(2)** as well stablished in the literature, the doping mechanism in graphene layers changes frequencies, linewidths and intensities of the G- and 2D-bands[39-47]. Most of the times, doping causes a frequency blueshift, a linewidth narrowing and an intensity decrease for the G-band, regardless of if the doping is a p- or n-type doping, while for the 2D-band the frequency may blueshift (redshift), the linewidth may narrow (broaden) and the intensity may decrease (increase) if the sample is p-doping (n-doping). All the 2D-band features will substantially change even under a low doping level[39-47]. Based on these facts, it is possible to conclude that the analysis of our Raman spectra do not follow **(1)** and **(2)**. Finally, the changes we observe could not be coming from defects neither because the increase (decrease) of defect densities is related to a broadening (narrowing) of every Raman band in carbon materials such as nanotubes, graphene layers and graphite but the frequencies associated to such Raman bands essentially do not change (except for cases in which the defect concentration is high)[48-51]. The absence of a D-band in our data indicates that the number of defects, if any, is small.

Quartz crystal microbalance experiments reveal that at 20 K, (Ar, Kr, and Xe) films are most likely completely pinned to pristine graphene[20]. It is known that the binding energy between heavier noble gases and the graphene sheet is higher[8,14]. As a result, the binding energies combined with the masses of these noble atoms (Ar with the

smallest mass and Xe with the highest mass), would potentially produce large and compressive biaxial strain in the graphene layer. Therefore, as discussed below, we hypothesize that in our experiments the noble gas forms a uniform adlayer adsorbed to the graphene surface and this adsorption produces compressive biaxial strain on the graphene sheet, which explains the blueshifts observed here. Hydrostatic, compressive and tensile biaxial or uniaxial strains cause significant modifications in the vibrational spectra for the G- and 2D-bands[32-36,52]. Under compressive biaxial/uniaxial strains or quasi-hydrostatic strains, both G and 2D-bands have their frequencies blue shifted[32-34]. On the other hand, uniaxial or biaxial tensile strains make the G and 2D-band frequencies decrease[35,36,52]. In the adsorption of gases at 20K, the frequencies of both, G and *2D*-bands are observed to upshift, which suggests that after adsorption, graphene is likely undergoing uniform/hydrostatic compressions or compressive biaxial strain rather than uniaxial/biaxial tensile strains. The magnitude of the shift is higher for the 2D-band when compare to the G-band, and both G- and 2D-band peak positions are different for adsorption of different noble gases, see Fig. 3(c).

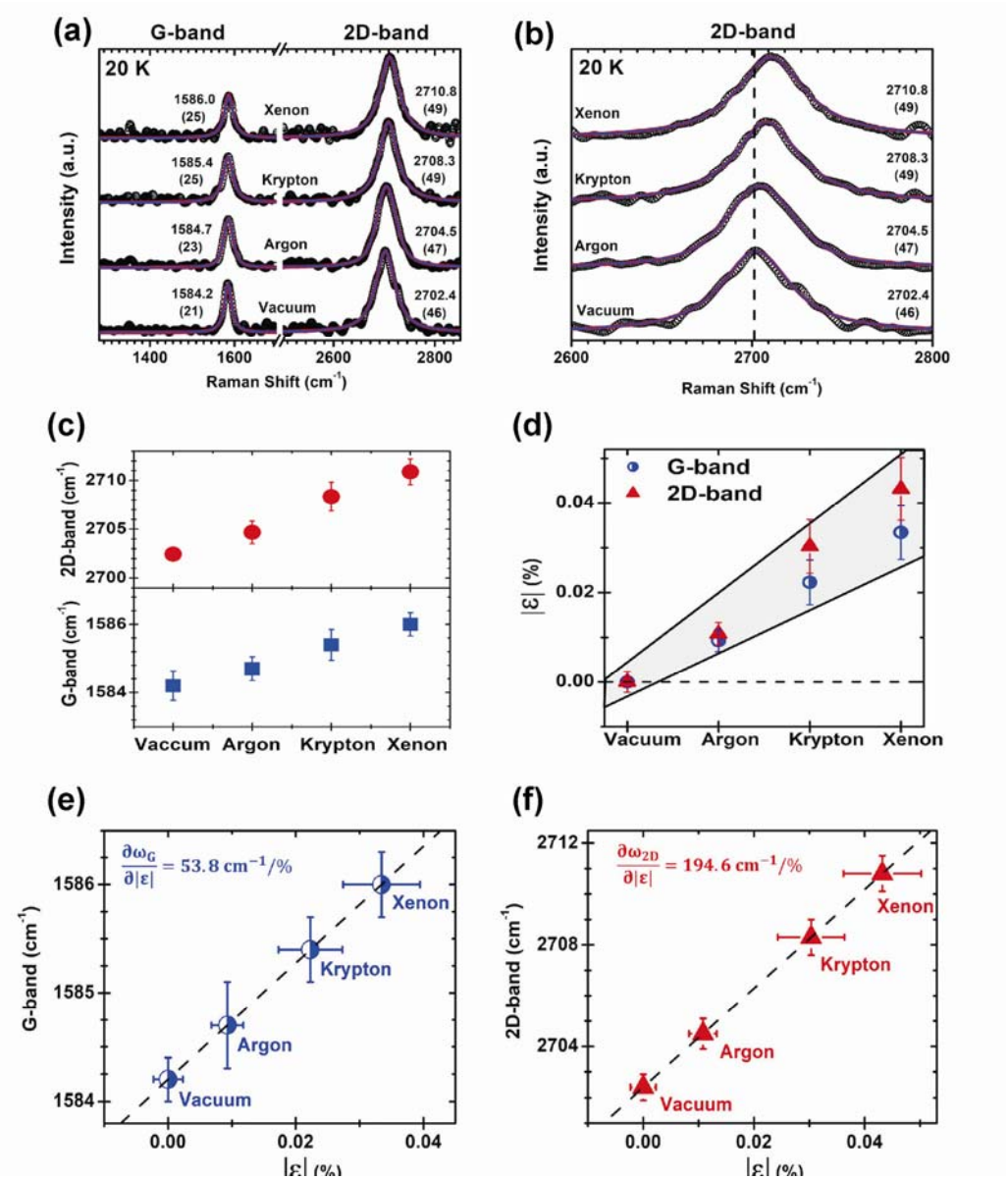

Fig. 3. (a) The G-band and 2D-band Raman spectra of single-layer graphene at 20K with 514.5 nm as the excitation wavelength. The spectra were collected under vacuum and after gas adsorption (Ar, Kr and Xe). **(b)** 2D-band highlighted so that the blue shifts are clearly visible (dotted lines are guides to the eyes for clarity of the shifts). **(c)** Evolution of position of the peaks from both G and *2D*-bands. **(d)** compressive strain of graphene by gas adsorption with different temperatures as a function of the gas type. (e) and (f) show, respectively, the G-band frequency and the 2D-band frequency as a function of the strain coefficient. From the graphics we obtain $\partial\omega_G/\partial|\varepsilon| = 53.8\,cm^{-1}/\%$ and $\partial\omega_{2D}/\partial|\varepsilon| = 194.6\,cm^{-1}/\%$. In (a) and (b), the black bullets are the experimental data and the solid lines are the fitting results (red) and the Lorentizian curves (blue) used to fit the data. The frequencies obtained from

the fittings are given by each peak and below them, between parentheses, the linewidths are given. The experimental errors for the frequencies and linewidths are, respectively, ±0.5 and ±1.

In the double-resonance phenomenon, which explains the 2D-band frequency appearing around 2700 cm^{-1} in the Raman spectra, each K (K') point has three neighboring K' (K) points and thus there are three scattering paths yielding equal contributions to the Raman shift due to the hexagonal symmetry of graphene as illustrated in Fig. 4[32,38]. In this situation, the 2D-band appears as a single peak for uncompressed graphene, as well established in the literature[32-36]. If the noble gas adlayer adsorbed on the graphene surface produces a homogeneous and uniform compression (biaxial compressions), the hexagonal symmetry of the lattice would be kept but every carbon-carbon bonding magnitude would be equally changed. In this case, the phonon dispersions would homogeneously modify along the three paths K (K'), keeping a single peak for both G- and 2D-band, which are blueshifted in frequency and present a small or negligible linewidth variation in comparison with the respective frequency and linewidth observed for uncompressed graphene[33,53-56]. Indeed, the effect of uniform compression (biaxial compressions) on the doubly degenerate G- band produces a blueshift in frequency and the lowering of the E_{2g} phonon symmetry does not happen (in other words just one G-band is observed), contrary to what happens in uniaxial tensile or compressive strains[33,53], where only a single peak (single G-band) is observed for small strains ($\varepsilon \leq 0.4$) but two peaks (often called G^+-band and G^--band) are observed as the strain increases ($\varepsilon > 0.4$).

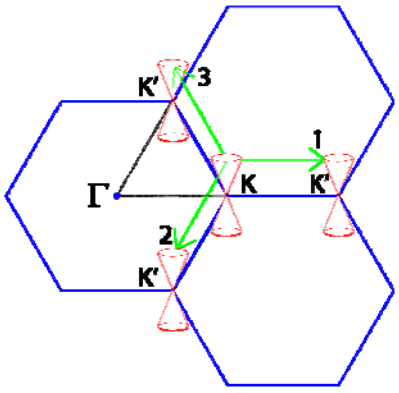

Fig. 4. Schematic representation of a double-resonant Raman-scattering process, which contributes for the *2D*-mode. An electron is scattered between the cone-like conduction bands at the *K* and *K'* points of the

hexagonal Brillouin zone of graphene by a *K*-point phonon with a wave vector, denoted by an arrow. The electron is scattered back by a phonon with an opposite wave vector. The three scattering paths KK' are denoted by 1, 2, and 3.

The mode-dependent relationship between the phonon mode frequency shift $\Delta\omega_{mode}$ and the strain coefficient, in the case of biaxial strains or uniform compression, is described by[33, 53-56]

$$\Delta\,\omega_{mode} = -2\omega^{0}_{mode}\gamma_{mode}\varepsilon \qquad (1)$$

.

In Eq. (01), "mode" stands for either the G-band or the 2D-band, ω^{0}_{G} (ω^{0}_{2D}) is the position of the G-band (2D-band) peak without any compressive strain $\omega^{0}_{G} = 1584.2\ cm^{-1}$ ($\omega^{0}_{2D} = 2702.4\ cm^{-1}$), $\gamma_G = 1.9$ ($\gamma_{2D} = 3.6$) are the Grüneisen parameters for the G-band (2D-band) and ε is the strain coefficient[33]. Thus, by using the Grüneisen parameter and the blueshift data of both G and 2D peaks, we can further estimate the compressive strains in the graphene due to the noble gases adsorption at 20K. As shown in Fig. 3(d), which plots modulus of strain coefficient |ε| as a function of the type of environment (vacuum, Ar, Kr and Xe), the values obtained for the strain coefficient range from 0.01% to 0.04%.

The coefficients ε extracted from the G-band data and from the 2D-band are in good agreement when taking into account the error bars. The small discrepancy comes from the fact that, as discussed above, the G-band is less sensitive to compressions, which increase the uncertainty on the coefficients determined with this band in comparison to the coefficients obtained with the 2D-band[53-56]. On top of that we are in regime of small strains (ε < 0.1%). Most importantly, the data is in very good agreement with what has been reported in the literature for biaxial compressive strains[53-56]. In order to further strength our interpretation, Figs. 3(e) and (f) plot, respectively, the G-band frequencies and the 2D-band frequencies as a function of |ε|. By fitting the data presented in Figs. 3(e) and (f) we obtain $\partial\omega_G/\partial|\varepsilon| = 53.8\ cm^{-1}/\%$ and $\partial\omega_{2D}/\partial|\varepsilon| = 194.6\ cm^{-1}/\%$. These rates are in very good agreement with biaxial compressions as reported in references 33 and 53 through 55. Such rates help us to exclude uniaxial compressions/tensile strains as the phenomena being observed since in these cases two

rates are expected for the G-band, $|\partial\omega_{G_{(-)}}/\partial|\varepsilon|| = (14.2 - 36.4)\ cm^{-1}/\%$ and $|\partial\omega_{G_{(+)}}/\partial|\varepsilon|| = (5.5 - 18.6)\ cm^{-1}/\%$, and for the 2D band $|\partial\omega_{2D}/\partial|\varepsilon|| = (70 - 83)\ cm^{-1}/\%$ (It is noticeable that such values are quite below what we observe) [33,53-55]. Indeed, by analyzing our data under the assumption that uniaxial strains are taking place (instead of biaxial compressions), the derivatives we obtain are quite different from what is reported in the literature for uniaxial strains, which further help us refute uniaxial strain as a possible explanation here. Table I summarizes the numerical results from our analysis comparing them with the literature.

Table I: Variations of the G-band and 2D-band frequencies as a function of the compressive strain $\partial\omega_G/\partial\varepsilon$. The values obtained in this work are compared with the literature.

$\frac{\partial\omega_{mode}}{\partial\lvert\varepsilon\rvert}\ \left(\frac{cm^{-1}}{\%}\right)$, for the G- and 2D-band					
Phonon mode	**Biaxial (compressive strain) (This work)**	**Biaxial (tensile strain)**	**Biaxial (compressive strain)**	**Uniaxial (tensile strain)**	**Uniaxial (compressive strain)**
G-band	53.8	-63[32] -57[54] -57.3[53]	57.3[53]	--	--
$G_{(+)}$-band	--	--		−18.6[32] -9.6[52]	5.5[52] 10.1[52]
$G_{(-)}$-band	--	--		−36.4[32] -31.4[52]	22.3[52] 31.1[52]
2D-band	194.6	-191[32] -140[54] -160.3[53]	160.3[53]	−83[32]	--

Before we describe the theoretical results to give further interpretation to the experimental work, it is worth reviewing some properties of noble gases adsorbed on graphite. At temperatures of 20 K and pressures of ~10^{-3} torr, the starting conditions of our measurements, the gases Ar, Kr, and Xe condense on graphite as a submonolayer up to a complete monolayer. All these atoms form triangular lattices on graphite but only Kr lattice is commensurate with the graphite basal plane and the other two form incommensurate lattices[2]. The interatomic noble gas distance within these adlayers has been reported to be larger than the value measured for the 3D noble gas solid for Ar and Kr, and shorter for Xe, so that these adlayers carry some amount of strain when adsorbed on graphite at low temperature. The structures of noble gases adsorbed on graphene are not known. Graphene has the same atomic structure as that of the graphite basal plane, however there is an important difference between these materials: graphene is atomically thin. The mechanical properties of this 2D material include a negative thermal expansion coefficient[57] and out-of-plane deformations leading to ripples[58]. The samples of the present work were deposited on a carbon film covered metallic grid at room temperature and then cooled down to very low temperatures for noble gas adsorption. Due to the different thermal expansion coefficients of graphene and the supporting grid, it is expected that, as the temperature lowers, the strain on the contacts and the expansion of the sample result in rippling of graphene at the suspended parts. The noble gas atoms condense in a corrugated substrate and should form islands in suspended graphene.

We now turn to the description of the DFT results. Figure 5 shows the optimized supercells containing, from left to right, 50 C and 9 Ar, 18 C and 3 Kr, and 50 C and 7 Xe. In terms of the graphene cell parameters, the initial noble gas atomic densities in these supercells are, respectively, 0.069 at/Å^2, 0.064 at/ Å^2, and 0.053 at/ Å^2. After optimization there is a small contraction of the supercell area, by 0.08% in the cells containing Ar and Xe, and by 0.03% in the cell containing Kr, which is equivalent to an average contraction of the cell parameter by 0.04% and 0.015%, respectively. This contraction could be due to the initial atomic densities assumed in the calculations, which are smaller than the corresponding values of the 2D noble gas solid. However, the supercell containing Kr atoms corresponds to the ideal Kr monolayer observed in graphite and still the cell contracts. Note that Kr occupies the hollow sites at the center of the carbon hexagons on the graphene lattice. The six C-C bonds connecting the Kr-

bearing ring to its neighbors are slightly contracted with respect to the other C-C bonds and, most importantly, graphene is no longer flat after Kr adsorption (and also after Ar and Xe adsorption). There is a small buckling, with the C atoms moving above and below the initial graphene plane.

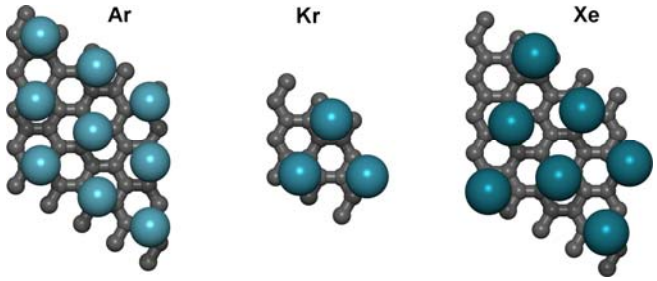

Fig. 5. Optimized supercells from M06L calculations: from left to right, 9 Ar atoms on a 5×5 graphene, 3 Kr atoms on a 3×3 graphene, and 7 Xe atoms on a 5×5 graphene.

This problem was further investigated by extending the calculations to larger supercells. The number of noble gas atoms chosen for the 10×10 supercells was that of a submonolayer, so that graphene is not completely covered by the adsorbates. We note that Ar and Xe monolayer lattices adsorbed on graphene, in analogy to what has been observed in graphite, are not expected to be commensurate with the graphene lattice, therefore a PBC calculation with a complete adsorbed monolayer of these gases on graphene is not possible. In order to make a fair comparison we adopted submonolayer coverages for all three gases. The initial geometry of the submonolayers was obtained by a classical molecular dynamics simulation at 20 K, using the NVT (constant number of particles N, constant volume V, constant temperature T) ensemble, and the force field *pcff* as implemented in the Materials Studio package. These input geometries were used in M06L and PBE-TS for the computation of ground state conformations. In general the optimized geometries from both DFT methods are similar. Differences are seen in the average interatomic distance of noble gas atoms and the distance of noble gas atoms to carbons, which are larger, by ~0.1 Å, in PBE-TS method, due to the different treatment of dispersion interactions in these methods. Figure 6 depicts three unit cells of the optimized geometries from M06L method, so that the pattern of noble gas adsorptions can be better represented. Carbon atoms were colored according to their height on the axis perpendicular to the figure, so that light blue is the lowest position and red is the

highest position. In these larger supercells the adatoms have more freedom to aggregate and some areas on graphene are not occupied.

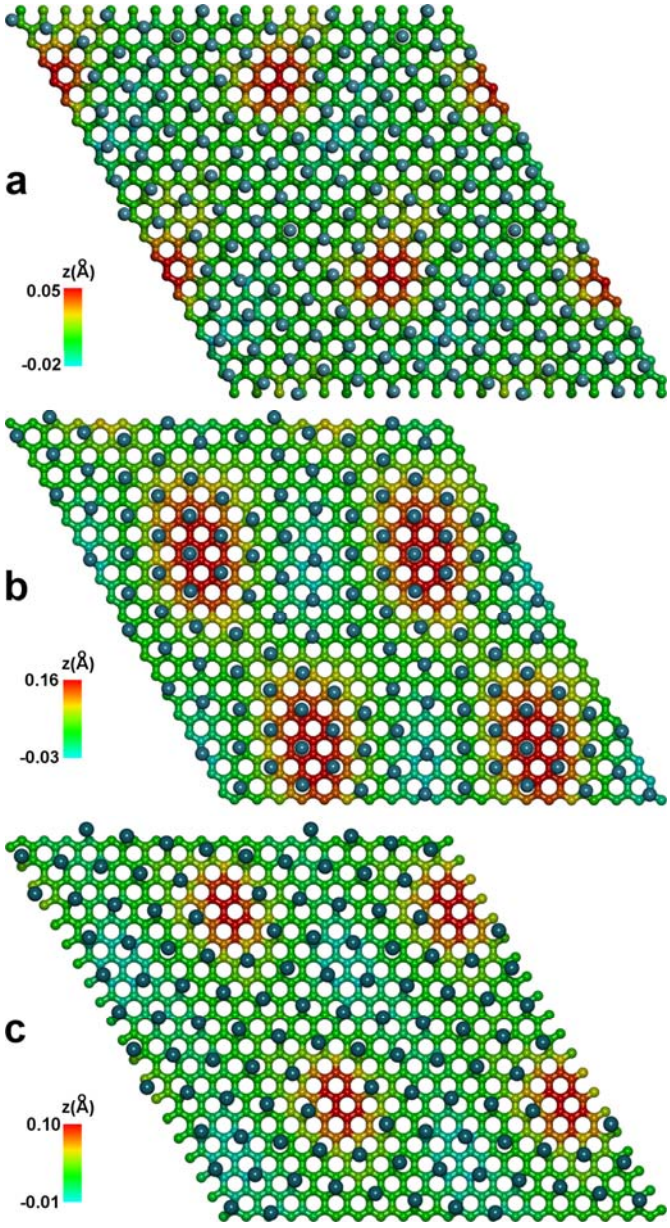

Fig. 6. Optimized 10×10 graphene supercells with submonolayers of noble gases from M06L calculations: **(a)** 36 Ar atoms per cell. **(b)** 32 Kr atoms per cell. **(c)** 29 Xe atoms per cell. Graphene is represented by the green structure, light blue is the lowest position and red is the highest position of the Carbon atoms, according to the bars of heights.

For Ar and Xe adsorption, the graphene regions not occupied by adatoms are higher (red) than the covered areas. A close look at Figs. 6a and 6c reveals that Ar and

Xe form quite regular triangular lattices with some empty areas due to the fractional coverage below 1. These noble gas lattices are also rotated with respect to graphene's symmetry axes, as has been observed for Ar and Xe monolayers in graphite at low temperatures[2]. The adsorption sites vary along a line of noble gas atoms, as in the incommensurate monolayer on graphite: the atoms can be found over a carbon atom, over a C-C bond, and near the center of a hexagon. This causes a small buckling of the carbon atoms (the blue-green areas in Fig. 6). At the edges of the empty areas the carbon atoms are attracted toward the noble gas island resulting in an elevation of the empty areas. The interatomic distances within the submonolayers are quite uniform unless for atoms near the empty areas, as expected. The mean values and standard deviations of interatomic distances are respectively 3.898 Å and 0.094 Å for Ar, while for Xe these values are 4.434 Å and 0.063 Å. For Kr, Fig. 6b, we see a quite different picture. The atoms occupy sites as in the commensurate Kr lattice (the center of carbon hexagons) above and near the red (higher) regions. In the blue-green (lower) regions the atoms form a disordered phase, as in a 2D liquid or 2D gas. The mean interatomic distance and the corresponding standard deviation are, respectively, 4.215 Å and 0.378 Å. Note the much higher standard deviation of interatomic distances in the Kr-graphene system as compared to the previous two cases, indicating some degree of disorder. This is also in agreement with experimental findings of a commensurate solid coexisting with a fluid phase in Kr over graphite at low temperatures ($T < 80$ K) and a fractional coverage below 1[2]. Compared to the calculated first neighbor distance of the corresponding 2D solids, Ar and Kr adlayers are dilated, whereas Xe adlayer is compressed, due to the interaction with graphene. The amplitude of the out-of-plane displacement of carbon atoms depends on the size of the areas without adatoms, the strength of the carbon-noble gas interaction, and on the commensurability of the noble gas lattice. These amplitudes in the present calculations are ~0.1 Å for Ar and Xe, and ~0.2 Å for Kr. An estimation of the fractional coverages using the calculated mean interatomic distances gave 0.90, 0.94, and 0.96, respectively, for Ar, Kr, and Xe, and the optimized graphene lattices at these fractional coverages are contracted, by 0.09%, 0.05% and 0.02%, respectively, mostly because of the buckling of carbon atoms, as seen in Fig. 6. These results suggest that not only the presence of adsorbed islands imparts strain on the graphene lattice, but also the size of the islands and the amount of uncovered surface have influence on the magnitude of the compression. For example,

the complete adlayer of Kr causes a 0.03% contraction of graphene surface while the fractional occupancy of 0.94 results in 0.05% contraction of the surface. It is noteworthy that these results are qualitatively the same in both calculation schemes, so that they neither depend on the type of basis set, the type of periodic boundary condition (2D or 3D), nor on the DFT functional and dispersion correction scheme.

The mobility of Ar, Kr, and Xe atoms on the surface at 20 K is low and decreases as the atomic mass increases. Therefore, at the same thermodynamic conditions, we should expect that Ar forms the largest adlayer islands and Xe the shortest islands, and also Xe adlayer must be made of more islands than Ar. The compressive strain caused by the adlayer-induced buckling of graphene thus depend on the number of these islands. As the temperature increases, the atomic mobility also increases, leading to the coalescence of neighboring islands and decreasing graphene buckling. The blue-shifts of graphene Raman bands as a function of the adsorbed noble gas and temperature are consistent with this picture.

In order to further understand the gas adsorption process, Raman spectra of suspended monolayer Nitrogen-doped graphene (NG) sheets with D-band to G-band intensity ratio ($I_D/I_G \sim 0.27$) using 514.5nm laser excitation were also acquired. The gas adsorption measurements on NG sheets were obtained under the same experimental conditions for the PG at 20K. The same rare gases, Ar, Kr and Xe were utilized to form the adlayers, as shown in Fig. 7(a) (Figure 7(b) shows the Raman spectrum zoomed into the 2D-band region). By incorporating nitrogen atoms into graphene, the physico-chemical properties of the graphene layer may be significantly altered depending on the doping configuration within the sub-lattices[16,17]. The substitutional doping of nitrogen within a graphene lattice forms a more electronegative covalent bonding with carbon atoms[16,59,60], which modifies the electronic structure of graphene. As discussed above, about 90% of the N atoms inserted in the graphene lattice assume the N_2^{AA} configuration. Nitrogen-doped graphene has a different response to noble gas adsorption (see Fig. 7). The local polarizability around a N-substituted site increases inside a radius of 1 nm[61]. It is likely that the noble gas atoms preferentially aggregate around the substitution sites and possibly form 3D structures. Figure 7(d) brings the NG Raman spectrum at 20K compared with the PG spectrum also at 20K. As seen for NG (and in accordance to Lv et al.[16]), the G-band and the 2D-band downshift, respectively, 1 cm^{-1}

and 4 cm^{-1} in comparison to the values observed for the PG. Such downshifts are signatures of doping effect in the graphene layer[62-65]. According to the literature[62.64,66], such downshifts correspond to an upshift of 350 meV in the Fermi level energy (E_F) of the system. It is known that the relation between E_F and the electron concentration in the system is: $E_F = \hbar|v_F|\sqrt{\pi n}$, where $\hbar$ is the Plank constant, $|v_F|$=1.1 X 10^6 ms^{-1}, and n is the electron concentration in cm^{-2}. Therefore, we estimate that the N-dopants introduce an electron concentration (n) of 0.5 X 10^{13} cm^{-2} (consistent with an N-doping concentration of 0.11at%)[16]. In average, electron concentrations of 0.5 X 10^{13} cm^{-2} correspond to an increase in the lattice-spacing variation of 0.01%.

As observed, the frequency blueshifts measured from PG upon gas adsorption are much higher than those observed on (NG) graphene. Indeed, as shown in Fig. 7(c) a significant upshift is seen only for the Xe adsorption case. Such upshifts correlate with the following strains in the NG layer: $|\varepsilon|$ = 0.025% for the D-band, $|\varepsilon|$ = 0.026% for the G-band and $|\varepsilon|$ = 0.016% for the 2D-band (all of them in good agreement by considering statistical errors). The observance of a meaningful upshift only for the Xe-adsorption case may be understood as follows: we have learned from the gas adsorption experiments on PG (Fig. 3) that: (1) upshifts of 0.5 cm^{-1} in the G-band (2 cm^{-1} in the 2D-band) require an average strain of 0.01% (this is the Ar adsorption case); (2) upshifts of 1 cm^{-1} in the G-band (5.9 cm^{-1} in the 2D-band) require an average strain of 0.025% (this is the Kr adsorption case); and (3) upshifts of 2 cm^{-1} in the G-band (8 cm^{-1} in the 2D-band) require an average strain of 0.037% (this is the Xe adsorption case). However, our NG leads to an increased lattice-spacing (0.01%) and to a decrease of 1 cm^{-1} in the G-band (4 cm^{-1} in the 2D-band). Therefore, in one hand, the N-doping leads to an increased lattice-spacing and to a downshift in frequency. On the other hand, uniform compressive strains (biaxial compressions) lead to a decreased lattice-spacing and to an upshift in frequency. This suggests that for NG, strains ≤ 0.025% in average, will not cause meaningful changes to the phonon mode frequencies. Therefore, we hypothesize that it is important to look at the overall effect involving the two different phenomena: biaxial compressive strain and doping. The presence of N-dopants even in small concentrations affects the uniform adsorption of the rare gases on graphene layer and compressions in the graphene layer are likely balancing (or being balanced by) the effects of doping due to the N dopants in the graphene layers.

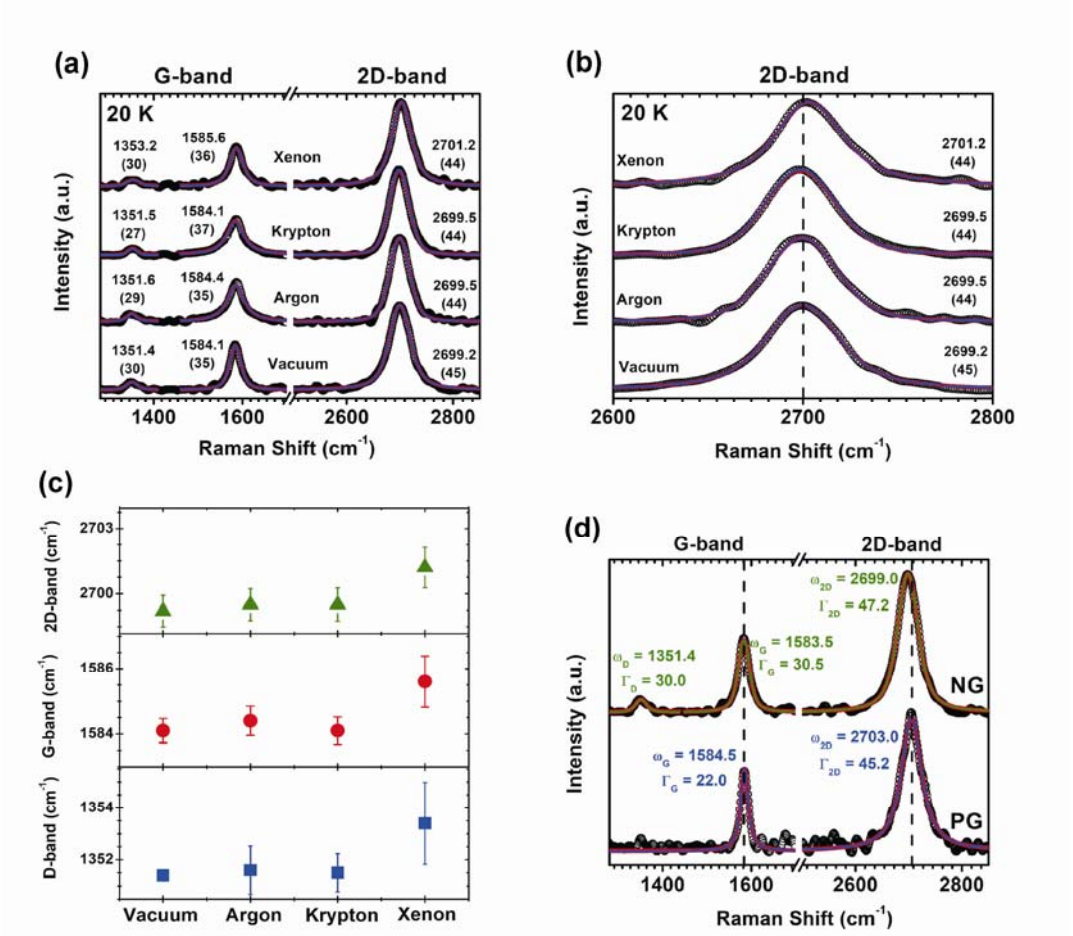

Fig. 7. (a) The D-band, G-band and 2D-band Raman spectra of single-layer Nitrogen-doped graphene at 20K with 514.5 nm as the excitation wavelength. The spectra were collected under vacuum and after gas adsorption (Ar, Kr and Xe). (b) 2D-band highlighted so that the blue shifts are clearly visible (dotted lines are guides to the eyes for clarity of the shifts). **(c)** Evolution of the peak position with respect to the gas adsorbed at the nitrogen-doped graphene surface. (d) Raman spectra for PG and NG at 20K. In (a), (b) and (d), the black bullets are the experimental data and the solid lines are the fitting results (red) and the Lorentizian curves (blue) used to fit the data. The frequencies obtained from the fittings are given by each peak and below them, between parentheses, the linewidths are given. The experimental errors for the frequencies and linewidths are, respectively, ±0.5 and ±1.

Next, gas desorption measurements on suspended PG were performed by increasing temperatures from 20K to 50K. It is important to emphasize that, once again, the frequency shifts for both G- and 2D-bands were monitored. Figure 8(a) shows the G- and 2D-band Raman spectra of Ar adlayer on PG at five different temperatures: 20K, 25K, 30K, 35K and 50K. The results indicate that with increasing temperature from 20K to 50K, the 2D-band Raman peak exhibits a downshift moving from 2704.5 to

2701.2 cm^{-1} (highlighted in Fig. 8(b)) and G-band frequency is slightly downshifted as well. However, for the Xe adsorption (Fig. 8(c)), when the temperature is increased from 20K to 50K, the 2D-band exhibit a much substantial frequency downshift ranging from 2710.8 to 2695.8 cm^{-1} (highlighted in Fig. 8(d)), while the G-band frequency downshifts from 1586 to 1581.2 cm^{-1}. To understand these downshifts, we must recall about the main mechanisms that contribute to frequency downshifts: **(1)** phonon anharmonicities and electron-phonon coupling changes due to increases in temperature[39,67-72], **(2)** Quasi-particles renormalizations and charge transfer between carbon and adsorbents[40-47], and **(3)** release of biaxial compressive strain and(or) uniaxial strains[35,36,52].

As regards (1), phonon anharmonicities and electron-phonon coupling changes due to increases in temperature, the main mechanisms behind the frequency shifts are the electron-phonon (e-ph) and the phonon-phonon (ph-ph) couplings. As vastly discussed in the literature, the ph-ph couplings come from lattice anharmonicities and contribute to changes in the phonon frequencies as the temperature changes. On the other hand, the e-ph couplings do not contribute as much to the lattice softening (hardening) as the temperatures decrease (increase). At very low temperatures, the e-ph contributions become even weaker and the ph-ph couplings, that become exponentially weaker, are basically the only contributors to change the phonon frequencies. Consequently, no meaningful changes in the phonon frequencies are expected due to increases in the temperature, which is in accordance with our measurements shown in Fig. 2(b). Indeed, it has been recently demonstrated (see Ref. 67) that the significant changes in the phonon frequencies happen in the range of temperatures from 200K to 400K. Our measurements are performed in the range of temperatures 20K – 50K, which is far below 200K – 400K, and this leads us to conclude that changes in phonon anharmonicities and electron-phonon couplings with increasing temperature should not be the reason for the observed frequency red-shifts. Moreover, if such changes were the effect behind the red-shifts, the G and 2D-bands for both, Ar/pristine graphene and Xe/pristine graphene cases would need to present similar behaviors. **Regarding (2)**, quasi-particles renormalizations and charge transfer between carbon and adsorbents, we point out that we are performing measurements of suspended graphene under high vacuum and the adsorbents are uncharged noble gases which are weakly interacting

with graphene through van der Waals interactions. Therefore, no charge transfer or quasi-particles renormalizations will occur.

Finally, we now present arguments to explain why **(3)** (release of compressive strain (biaxial compression)), might be the reason behind the frequency redshifts. First, we note that, according to Fig. 3 (a), before the adsorptions of the gases at 20K, the pristine G-band frequency was 1584.2 cm^{-1} and the pristine 2D-band frequency was 2702.4 cm^{-1}. Secondly, at this temperature an incommensurate adlayer in the solid phase for both Ar and Xe adsorbed on the carbon surface is expected, which is confirmed by our calculations (see Fig. 6 (a), (b) and (c)), and other works published in the literature[73-80]. This incommensurate phase is an organized phase for both Ar and Xe whose densities are expected to be homogeneous and high enough to form the solid structures, which explains the compressive strain on the PG. As the temperature is increased from 20K to 50K, we note that the G- and 2D-band frequencies tend to return to their pristine values, which we attribute to a deppining of adsorbates from the PG layer. Figures 8(e) and (f) show the evolution of the peaks positions for Ar/PG and Xe/PG. For Xe/PG, as shown in Fig. 8(f), after 35 K changes in the Raman frequency seem to be decreasing with a slower rate. These data indicate a thermal depinning transition with a characteristic temperature around 35K for Xe/PG. The slippage of Ar/PG seems to be different from that observed on Xe/PG. As shown in Fig. 8(e), around 30K no significant shifts are observed indicating that in this case the depinning starts at a lower temperature when compared to the Xe/PG case, which reflects the smaller polarizability of the Ar atoms. For Kr/PG, the depinning starts at an even lower temperature: 25K (see Supplemental Material [22]). Our results are in good agreement with those reported by Pierno *et al.*[20]. We now use our results to evaluate the changes in the observed strains with increasing temperature from 20K to 50K (the Supplemental Material section provides the corresponding results from Kr adsorption as Fig. S1 [22]). Figures 8(g) and (h) show the temperature-driven downshifts of the G- and 2D-band, respectively, as a function of the biaxial strain calculated using Eq. (1). In both figures, the green symbols stand for the Ar/PG data; the wine symbols stand for the Kr/PG data; and the blue symbol stand for the Xe/PG data. The results for Ar/PG are shown in the insets. In overall, the results are rather interesting: there is a clear transition from compressive biaxial strains (see the transparent-blue region in the graphics) to tensile

biaxial strains (see the transparent-red region in the in the graphics). Both, figures and respective insets, show that black solid line fitting the data have approximately the same slopes observed earlier in Fig. 3, indicating that we are indeed observing biaxial strains. The dashed horizontal and vertical lines mark the G- and 2D-band frequencies for PG, which would present null strain. *We would like to emphasize that a detailed explanation for such transition will be addressed elsewhere*.

However, inspired by the literature, we would like to offer an explanation for what is likely taking place, which is based on the slippage of noble gas structures on PG surface: the incommensurate phase of Xe and Ar on PG consist of commensurate and incommensurate domains, where commensurate domains are separated by incommensurate domains. This happens because the noble gas structure formed at 20K and PG possess nonmatching lattice parameters, which is in accordance with our calculations. As mentioned by Pierno *et al.*[20], such domain structures are governed by the competition in minimizing both interfacial energy and elastic strain energy. When the size of the contact between domains is reduced below a critical value, such domains may coalesce and lead to a sharp increase of the interfacial commensurability. However, depinning of commensurate domains is a thermal activated process and becomes very likely as such domains get larger. Therefore, the temperature-driven slippage of the incommensurate layers could be explained by the increase of commensurability of the constituent domains. Small domains would stay pinned while larger domains created from merged domains would undergo depinning and slippage. The results for Krypton corroborate the explanation since they already form commensurate structures after adsorption and have the lowest deppining temperature. The depinning likely has a mass dependence effect as well because any small increase in the thermal energy is already enough for the adsorbed atoms to oscillate and acquire kinetic energy to overcome the weak potential barrier between the graphene layer and adsorbates, dominated by weak van der Waals interactions. Since Ar atoms are much lighter than Xe atoms, the barrier is more easily overcome for Ar atoms[81-83]. As mentioned earlier in the text, our simulations suggest the size and distribution of the domains together with the amount of uncovered surface have influence on the type and magnitude of the strains. Therefore, as the temperature increases the domain distribution and number of adsorbates change,

which also modifies the PG adsorbate coverage and is potentially the reason for the transition from a compressive to a tensile biaxial strain.

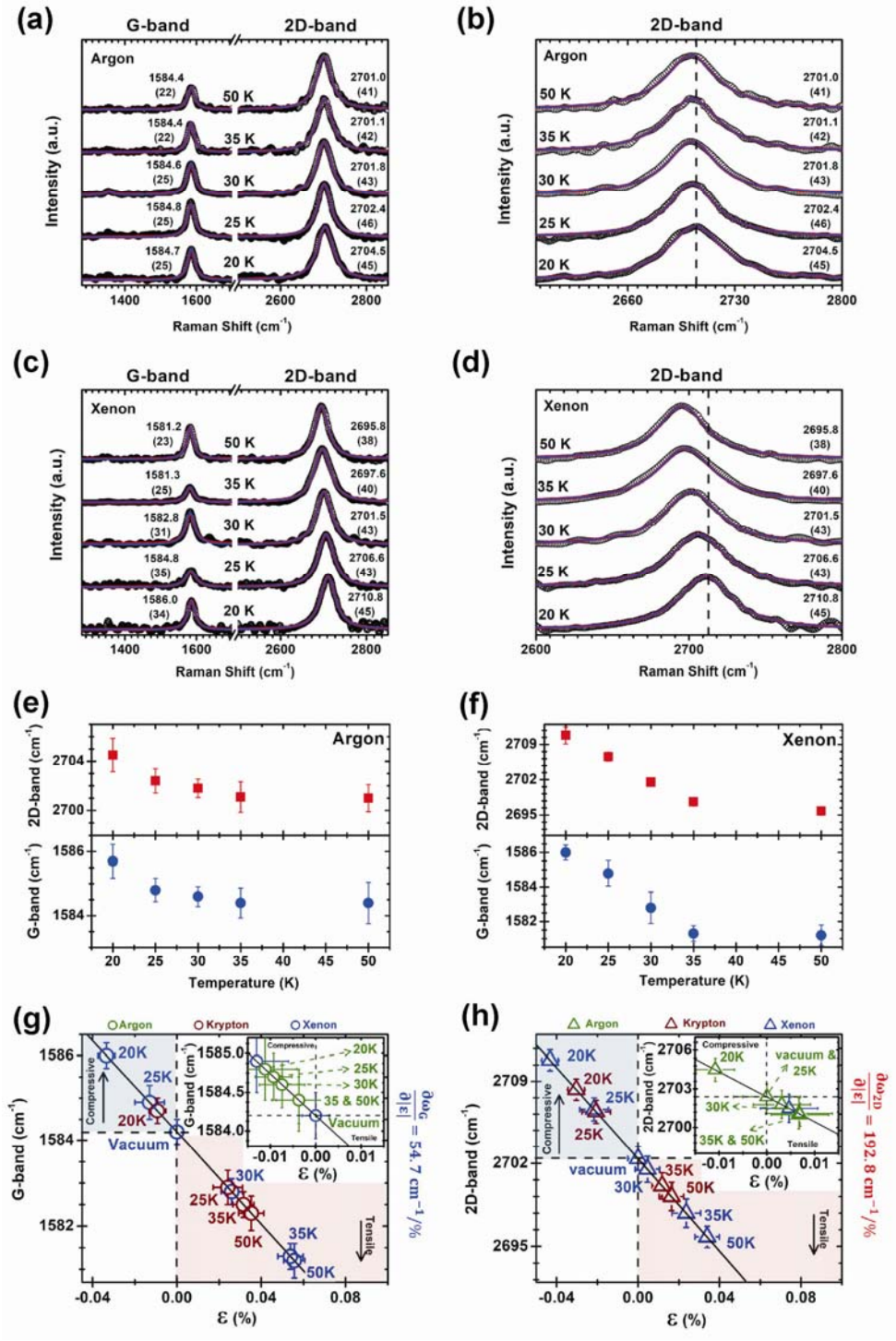

Fig. 8. The G-band and *2D*-band Raman spectra of pristine single-layer graphene at different temperatures with 514.5 nm as the excitation wavelength. (a) and (b) Ar/PG Raman spectra evolution

with increasing temperature. (c) and (d) Xe/PG Raman spectra evolution with increasing temperature. (e) and (f) Evolution of the G- and 2D-bands peak position, respectively, as a function of temperature. (g) and (h) temperature-driven downshifts of the G- and 2D-band, respectively, as a function of the biaxial strain. In (a) through (d), the black bullets are the experimental data and the solid lines are the fitting results (red) and the Lorentizian curves (blue) used to fit the data. The frequencies obtained from the fittings are given by each peak and below them, between parentheses, the linewidths are given. The experimental errors for the frequencies and linewidths are, respectively, ±0.5 and ±1.

4. Conclusions

In summary, we have shown that the adsorption of rare gases (Ar, Kr and Xe) on suspended monolayers of pristine graphene at low temperature produces compressive strains on the graphene layer. This compression is larger for the system Xe/PG due the higher polarizability of this adsorbate when compared to Kr and Ar. However, for N-doped graphene the compression using the same rare gases is less due to not uniform distribution of the adatoms on N-doped sheets. Moreover, we hypothesize that biaxial compressive strains and doping are two effects that balance each other. These results are supported by Raman spectroscopy measurements and density functional theory calculations. Furthermore, we have shown the behavior of the gas adsorption on suspended monolayer graphene at higher temperatures. In this case the G- and 2D-band frequencies tend to downshift to values below the pristine values as result of a thermal activated slippage and depinning transition that leads to a change from biaxial compressive strain to biaxial tensile strains. We believe that our method could be exploited further in order to quantify the amount of strain and to study depinning transition of adsorbed films, providing a fundamental tool for graphene-based nanoelectronics mechanical systems.

Acknowledgments

This work was financially supported by the US Air Force Office of Scientific Research MURI grant FA9550-12-1-0471. R.C., N.P.L., A.L.E. and M.T. acknowledge the financial support from the U.S. Army Research Office through the MURI grant W911NF-11-1-0362. P. T. A. acknowledges the College of Arts and Sciences at the

University of Alabama for supporting this research through startup money funds. The authors acknowledge the National Science Foundation for financial support under grants EFRI-1433311 (A.L.E.) and EFRI-1433378 (M.T.). M.C.S. acknowledges FAPESP for financial support and the Research Computing and Cyber-infrastructure unit of Information Technology Services at Penn State University for providing access to the advanced computational facilities and services. R.C. acknowledges the scholarship CNPq/PDE (234973/2014-5).

References

1. A. M. DaSilva and M. W. Cole, Effects of Physically Adsorbed Films on Conductivity of Two-Dimensional Metal Surfaces and Graphene, J. Low Temp. Phys.163, 122 (2011).
2. L. W. Bruch, M. W. Cole, E. Zaremba, and Physics, Physical Adsorption: Forces and Phenomena (Claredon Press, Oxford, 1997).
3. C. Kittel and H. Kroemer, Thermal Physics (W. H. Freeman and Company, New York, 1980), 2nd ed.
4. H.Tercas, S. Ribeiro and J. T. Mendonca, Quasi-Polaritons in Bose–Einstein Condensates Induced by Casimir–Polder Interaction with Graphene, J. Phys. Condens. Matter, 27, 214011 (2015).
5. K. Nakada and A. Ishii, DFT Calculation for Adatom Adsorption on Graphene, Graphene Simulation (Prof. Jian Gong (Ed.), InTech, 2011).
6. A.Ambrosetti and P. L.Silvestrelli, Adsorption of Rare-Gas Atoms and Water on Graphite and Graphene by van der Waals-Corrected Density Functional Theory, J. Phys. Chem. C 115, 3695 (2011).
7. M. Foroutan and A. T.Nasrabadi, Adsorption and Separation of Binary Mixtures of Noble Gases on Single-Walled Carbon Nanotube Bundles, Physica E 43, 851 (2011).
8. M. Neek-Amal and A. Lajevardipour, Stochastic Motion of Noble Gases on a Graphene Sheet, *Comput. Mater. Sci.* 49, 839 (2010).

9. S. M. Maiga and S. M. Gatica, Monolayer Adsorption of Noble Gases on Graphene,cond-mat.mtrl-sci. arXiv: 1609.01989v1 (2016).
10. Z. Wang, J. Wei, P. Morse, J. G. Dash, O. E. Vilches, D. H. Cobden, Phase Transitions of Adsorbed Atoms on the Surface of a Carbon Nanotube, *Science* 327, 552 (2010).
11. J. G. Dash and J.Ruvalds, Phase Transitions in Surface Films, (NATO Advanced Study Institute Series B, Plenum Press, New York, 1980).
12. M. Foroutan and A. T. Nasrabadi, Adsorption Behavior of Ternary Mixtures of Noble Gases Inside Single-walled Carbon Nanotube Bundles, *Chem. Phys. Lett.* 497, 213 (2010).
13. F. Schedin, A. K. Geim, S. V. Morozov, E. W. Hill, P. Blake, M. I. Katsnelson and K. S. Novoselov, Detection of individual gas molecules adsorbed on graphene. *Nat. Mater.* 6, 652 (2007).
14. E. Bichoutskaia, and N. C. Pyper, A Theoretical Study Of The Cohesion Of Noble Gases On Graphite. *J. Chem. Phys.*128, 024709 (2008).
15. S. Jalili and R. Majidi, The Effect of Gas Adsorption on Carbon Nanotubes Properties. *J. Comput. Theor. Nanosci.* 3, 664 (2006).
16. R. Lv, Q. Li, A. R. Botello-Mendez, T. Hayashi, B. Wang, A. Berkdemir, Q. Hao, A. L. Elıas, R. Cruz-Silva, H. R. Gutierrez, Y. A. Kim, H. Muramatsu, J. Zhu, M. Endo, H. Terrones, J.C. Charlier, M. Pan and M. Terrones, Nitrogen-doped graphene: beyond single substitution and enhanced molecular sensing. *Sci. Rep.* 2, 586 (2012).
17. H., Lv, R., Terrones, M. Terrones, and M. S. Dresselhaus, The Role Of Defects And Doping In 2D Graphene Sheets And 1D Nanoribbons. Rep. Prog. Phys.75, 062501 (2012).
18. J. Rintala, O. Herranen, A. Johansson, M. Ahlskog, and M. Pettersson, Raman Spectroscopy And Low-Temperature Transport Measurements Of Individual Single-Walled Carbon Nanotubes With Varying Thickness. J. Phys. Chem. C 113, 15398 (2009).
19. L. Zhang, Z. Jia, L. Huang, S. O'Brien, and Z. Yu, Low-Temperature Raman Spectroscopy Of Individual Single-Wall Carbon Nanotubes And Single-Layer Graphene. J. Phys. Chem. C 112, 13893 (2008).
20. M. Pierno, L. Bignardi, M. C.Righi, L. Bruschi, S. Gottardi, M. Stohr, O. Ivashenko,

P. L. Silvestrelli, P. Rudolf and G. Mistura, Thermolubricity of gas monolayers on graphene. Nanoscale 6, 8062 (2014).

21. Y. N. Zhang, V. Bortolani, and G. Mistura, Influence Of Graphene Coating On The Adsorption And Tribology Of Xe On Au (1 1 1) Substrate. J. Phys. Condens. Matter 26, 445003 (2014).
22. See Supplemental Material at http://..... for a brief description of temperature-dependent Raman scattering and for the results of Krypton desorption with increasing temperature.
23. Y. Zhao, D.G. Truhlar, A New Local Density Functional For Main-Group Thermochemistry, Transition Metal Bonding, Thermochemical Kinetics, And Noncovalent Interactions. J. Chem. Phys. 125, 194101 (2006).
24. J.G. Hill, S. Mazumder, and K.A. Peterson, Correlation Consistent Basis Sets For Molecular Core-Valence Effects With Explicitly Correlated Wave Functions: The Atoms B–Ne And Al–Ar. J. Chem. Phys. 132, 054108 (2010).
25. J.G. Hill, and K.A. Peterson, Correlation Consistent Basis Sets For Explicitly Correlated Wavefunctions: Pseudopotential-Based Basis Sets For The Post-D Main Group Elements Ga–Rn. J. Chem. Phys. 141, 094106 (2014).
26. K. A. Peterson, D. Figgen, E. Goll, H. Stoll, M. Dolg, Systematically Convergent Basis Sets With Relativistic Pseudopotentials. II. Small-Core Pseudopotentials And Correlation Consistent Basis Sets For The Post-D Group 16–18 Elements. J. Chem. Phys. 119, 11113 (2003).
27. Gaussian 09 (Gaussian, Inc., Wallingford, CT, USA, 2009).
28. J. P. Perdew, K. Burke, and M. Ernzerhof, Generalized Gradient Approximation Made Simple. *Phys. Rev. Lett.* 77, 3865 (1996).
29. A. Tkatchenko, M. Scheffler, Accurate Molecular Van Der Waals Interactions From Ground-State Electron Density And Free-Atom Reference Data. *Phys. Rev. Lett.* 102, 073005 (2009).
30. S. J. Clark, M. D. Segall, C. J. Pickard, P. J. Hasnip, M. J. Probert, K. Refson, M. C. Payne, First Principles Methods Using CASTEP. *Z. Kristallographie* 220, 567 (2005).
31. Accelrys Software Inc., Materials Studio Release Notes, Release 6.1,Accelrys Software Inc., San Diego, 2012.

32. D. Yoon, Y.-W. Son, and H. Cheong, Strain-Dependent Splitting Of The Double-Resonance Raman Scattering Band In Graphene. *Phys. Rev. Lett.*106, 155502 (2011).
33. T. M. G. Mohiuddin, A. Lombardo, R. R. Nair, A. Bonetti, G. Savini, R. Jalil, N. Bonini, D. M. Basko, C. Galiotis, N. Marzari, K. S. Novoselov, A. K. Geim, A. C. Ferrari, Uniaxial strain in graphene by Raman spectroscopy: G peak splitting, Grüneisen parameters, and sample orientation. Phys. Rev. B 79, 205433 (2009).
34. M. Huanga, H. Yanb, C. Chena, D. Songb, T. F. Heinz and J. Honea, Phonon softening and crystallographic orientation of strained graphene studied by Raman spectroscopy. *Proc. Natl. Acad. Sci.*106, 7304 (2009).
35. S. M. Clark, K.-J. Jeon, J.-Y. Chen, and C.-S. Yoo, Few-Layer Graphene Under High Pressure: Raman And X-Ray Diffraction Studies. Solid State Commun.154, 15 (2013).
36. K. Filintoglou, N. Papadopoulos, J. Arvanitidis, D. Christofilos, O. Frank, M. Kalbac, J. Parthenios, G. Kalosakas, C. Galiotis and K. Papagelis, Raman spectroscopy of graphene at high pressure: Effects of the substrate and the pressure transmitting media. *Phys. Rev. B* 88, 045418 (2013).
37. M. Mohr, J. Maultzsch, and C. Thomsen, Splitting Of The Raman 2D Band Of Graphene Subjected To Strain. Phys. Rev. B 82, 201409 (2010).
38. V. N. Popov, and P. Lambin, Theoretical 2D Raman Band Of Strained Graphene. Phys. Rev. B 87, 155425 (2013).
39. D. L. Mafra, J. Kong, K. Sato, R. Saito, M. S. Dresselhaus and P. T. Araujo**,** Using the G′ Raman Cross-Section To Understand the Phonon Dynamics in Bilayer Graphene Systems. *Nano Lett.*12, 2883 (2012).
40. D. L. Mafra, and P. T. Araujo, Intra- And Interlayer Electron-Phonon Interactions In 12/12C And 12/13C Bilayer Graphene. *Appl. Sci.*4, 207 (2014).
41. R. Saito, K. Sato, P. T. Araujo, D. L. Mafra and M. S. Dresselhaus, Gate Modulated Raman Spectroscopy Of Graphene And Carbon Nanotubes. *Solid State Commun.*175, 18 (2013).
42. P. T. Araujo, D. L. Mafra, K. Sato, R. Saito, J. Kong and M. S. Dresselhaus, Phonon Self-Energy Corrections to Nonzero Wave-Vector Phonon Modes in Single-Layer Graphene. *Phys. Rev. Lett.*109, 046801 (2012).

43. P. T. Araujo, M. Terrones, and M. S. Dresselhaus, Defects And Impurities In Graphene-Like Materials. *Mater.* Today 15, 98 (2012).
44. D. L. Mafra, J. Kong, K. Sato, R. Saito, M. S. Dresselhaus and P. T. Araujo, Using gate-modulated Raman scattering and electron-phonon interactions to probe single-layer graphene: A different approach to assign phonon combination modes. *Phys.* Rev. B 86, 195434 (2012).
45. L. S. Panchakarla, K. S. S. Synthesis, Structure, and Properties of Boron- and Nitrogen-Doped Graphene. *Adv. Mater.* 21, 4726 (2009).
46. X. Mei, X. Meng and F. Wu, Evolution Of The Raman Properties Of Nitrogen-Doped Graphene Sheets With Reducing Agent. *Eur. Phys. J. Appl. Phys.*70, 10402 (2015).
47. G. Froehlicher and S. Berciaud, Raman Spectroscopy Of Electrochemically Gated Graphene Transistors: Geometrical Capacitance, Electron-Phonon, Electron-Electron, And Electron-Defect Scattering, *Phys. Rev. B* 91, 205413 (2015).
48. L. G. Cançado, A. Jorio, E. H. Martins Ferreira, F. Stavale, C. A. Achete, R. B. Capaz, M. V. O. Moutinho, A. Lombardo, T. S. Kulmala and A. C. Ferrari, Quantifying Defects In Graphene Via Raman Spectroscopy At Different Excitation Energies. *Nano Lett.*, 11 (8), 3190 (2011).
49. M. S. Dresselhaus, A. Jorio, A. G. Souza Filho and R. Saito, Defect Characterization In Graphene And Carbon Nanotubes Using Raman Spectroscopy. Phil. Trans. R. Soc. A 368, 5355 (2010).
50. G. D. Saraiva, A. G. Souza Filho, G. Braunstein, E. B. Barros, J. Mendes Filho, E. C. Moreira, S. B. Fagan, D. L. Baptista, Y. A. Kim, H. Muramatsu, M. Endo and M. S. Dresselhaus, Resonance Raman Spectroscopy In Si And C Ion-Implanted Double-Wall Carbon Nanotubes. Phys. Rev. B 80, 155452 (2009).
51. S. Osswald, M. Havel, Y. Gogotsi, Monitoring Oxidation Of Multiwalled Carbon Nanotubes By Raman Spectroscopy. J. Raman Spectrosc. 38, 728 (2007).
52. D. Abbasi-Pérez, J. M. Menéndez, J. M. Recio, A. Otero-de-la-Roza, E. del Corro, M. Taravillo, V. G. Baonza and M. Marqués, Modeling graphite under stress: Equations of state, vibrational modes, and interlayer friction. Phys. Rev. B **90,** 054105 (2014).

53. O. Frank, G. Tsoukleri, J. Parthenios, K. Papagelis, I. Riaz, R. Jalil, S. Kostya K. S. Novoselov and C. Galiotis, Compression Behavior of Single-Layer Graphenes. ACSnano 4 (6), 3131 (2010).

54. F, Ji H., Ding, Y. Chen, A. Herklotz, K. Dörr, Y. Mei, A. Rastelli and O. G. Schmidt, Stretchable Graphene: A Close Look at Fundamental Parameters through Biaxial Straining. *Nano Lett.*, 10 (9), 3453 (2010).

55. J. Zabel, R. R. Nair, A. Ott, T. Georgiou, A. K. Geim, S. Kostya, K. S. Novoselov and C. Casiraghi, Raman Spectroscopy of Graphene and Bilayer under Biaxial Strain: Bubbles and Balloons.*Nano Lett.* 12 (2), 617 (2012).

56. J. E. Proctor, E. Gregoryanz, K. S. Novoselov, M. Lotya, J. N. Coleman, and M. P. Halsall, High-Pressure Raman Spectroscopy Of Graphene. Phys. Rev. B 80, 073408 (2009).

57. V. Singh, S. Sengupta, H. S. Solanki, R. Dhall, A. Allain, S. Dhara, P. Pant and M. M. Deshmukh, Probing Thermal Expansion Of Graphene And Modal Dispersion At Low-Temperature Using Graphene Nanoelectromechanical Systems Resonators. *Nanotechnology***21**, 165204 (2010).

58. C.-C. Chen, W. Bao, J. Theiss, C. Dames, C. N. Lau and S. B. Cronin, Raman Spectroscopy of Ripple Formation in Suspended Graphene. *Nano Letters* **9** (12), 4172 (2009).

59. L. He, R. Zhao, K. T. Rim, T. Schiros, K. S. Kim, H. Zhou, C. Gutiérrez, S. P. Chockalingam, C. J. Arguello, L. Pálová, D. D. Nordlund, M. S. Hybertsen, D. R. Reichman, T. F. Heinz, P. Kim, A. Pinczuk, G. W. Flynn, A. N. Pasupathy, Visualizing Individual Nitrogen Dopants in Monolayer Graphene. Science 333 (6045), 999 (2011).

60. D., Deng, X., Pan, Yu, L., Y. Cui, Y. Jiang, J. Qi, W. X. Li, Q. Ma, X. Fu, Q. Xue, G. Sun and X. Bao, Toward N-Doped Graphene via Solvothermal Synthesis. *Chem. Mater.* 23 (5), 1188 (2011).

61. V. D. Pham, V. Repain, C. Chacon, A. Bellec, Y. Girard, S. Rousset, R. Sporken, M. C. dos Santos and J. Lagoute, Molecular Adsorbates As Probes Of The Local Properties Of Doped Graphene. *Sci. Rep*. **6**, 24796 (2016).

62. M. Lazzeri and F. Mauri, Nonadiabatic Kohn Anomaly in a Doped Graphene Monolayer. Phys. Rev. Lett. 97, 266407 (2006).

63. N., Caudal, A. M., Saitta, M., Lazzeri and F. Mauri, Kohn Anomalies And Nonadiabaticity In Doped Carbon Nanotubes. Phys. Rev. B 75, 115423 (2007).

64. A. D. B. Chakraborty, S. Piscanec, S. Pisana, A. K. Sood and A. C. Ferrari, Phonon Renormalization In Doped Bilayer Graphene. Phys. Rev. B 79, 155417 (2009).

65. H. Farhat, K. Sasaki, M. Kalbac, M. Hofmann, R., Saito, M. S. Dresselhaus and J. Kong, Softening of the Radial Breathing Mode in Metallic Carbon Nanotubes. Phys. Rev. Lett. 102, 126804 (2009).

66. A., Das, S. Pisana, B. Chakraborty, S. Piscanec, S. K. Saha, U. V. Waghmare, K. S. Novoselov, H. R. Krishnamurthy, A. K. Geim, A. C. Ferrari and A. K. Sood, Monitoring Dopants By Raman Scattering In An Electrochemically Top-Gated Graphene Transistor. Nature Nanotechnology 3, 210 (2008).

67. D. Yoon, Y.-W. Son and H. Cheong, Negative Thermal Expansion Coefficient of Graphene Measured by Raman Spectroscopy. *Nano Lett.***11,** 3227 (2011).

68. A. A. Balandin, S. Ghosh, W. Bao, I. Calizo, D. Teweldebrhan, F. Miao and C. N. Lau, Superior Thermal Conductivity of Single-Layer Graphene. *Nano Lett.* **8,** 902 (2008).

69. K. T. Nguyen, D. Abdula, C.-L. Tsai and M. Shim, Temperature And Gate Voltage Dependent Raman Spectra Of Single-Layer Graphene. *ACS Nano* **5,** 5273 (2011).

70. M. J. Allen, J. D. Fowler, V. C. Tung, Y. Yang, B. H. Weiller and R. B. Kaner, Temperature dependent Raman spectroscopy of chemically derived graphene. *Appl. Phys. Lett.* **93,** 193119 (2008).

71. J.-U. Lee, D. Yoon, H. Kim, S. W. Lee and H. Cheong, Thermal Conductivity Of Suspended Pristine Graphene Measured By Raman Spectroscopy. *Phys. Rev. B* **83,** 081419 (2011).

72. S. Berciaud, S. Ryu, L. E. Brus and T. F. Heinz, Probing The Intrinsic Properties Of Exfoliated Graphene: Raman Spectroscopy Of Free-Standing Monolayers. *Nano Lett.* 9**,** 346 (2009).

73. A. Patrykiejew, Phase Behavior Of Mixed Ar–Kr, Ar–Xe And Kr–Xe Monolayer Films On Graphite: A Monte Carlo Study. *J. Phys. Condens. Matter* **25,** 015001 (2013).

74. V. T. Nguyen, D. D. Do and D. Nicholson, On the Heat of Adsorption at Layering Transitions in Adsorption of Noble Gases and Nitrogen on Graphite. *J. Phys. Chem. C* 114**,** 22171 (2010).

75. E. D. Specht, M. Sutton, R. J. Birgeneau, D. E. Moncton and P. M. Horn, Phase Diagram And Phase Transitions Of Krypton On Graphite In The One-To-Two-Layer Regime. *Phys. Rev. B* 30**,** 1589 (1984).

76. M. Henderson and M. S. Wertheim, Phase Diagram and pV Isotherms of Argon. *J. Chem. Phys*. **51,** 5420 (1969).

77. E. A. Ustinov and D. D. Do, Simulation Study Of Two-Dimensional Phase Transitions Of Argon On Graphite Surface And In Slit Micropores. *Adsorption* **20,** 439 (2013).

78. P. Day, M. Lysek, M. LaMadrid and D. Goodstein, Phase Transitions In Argon Films. *Phys. Rev. B***47,** 10716 (1993).

79. J. Zheng, Q. F. Chen, Y. J. Gu, Z. Y. Chen and C. J. Li, Thermodynamics, Compressibility, And Phase Diagram: Shock Compression Of Supercritical Fluid Xenon. *J. Chem. Phys.* **141,** 124201 (2014).

80. G. L. Pollack, The Solid State of Rare Gases. Rev. Mod. Phys. 36, 748 (1964).

81. D. A. McQuarrie, Statistical Mechanics. (Harper and Row, New York 1976).

82. H. Wise and J. Oudar, Materials Concepts in Surface Reactivity and Catalysis. (Dover Publications, New York 2001).

83. Y. W. Chung, Practical Guide to Surface Science and Spectroscopy. (Academic Press, California 2001).

84. N. Bonini, M. Lazzeri, N. Marzari and F. Mauri, Phonon Anharmonicities in Graphite and Graphene. Phys. Rev. Lett. 99, 176802 (2007).

85. S. Tian, Y.Yang, Z. Liu, C. Wang, R. Pan, C. Gu and J. Li, Temperature-Dependent Raman Investigation on Suspended Graphene: Contribution From Thermal Expansion Coefficient Mismatch Between Graphene and Substrate. Carbon 104, 27 (2016).